THE JOURNAL OF PHYSICAL CHEMISTRY C

Article

pubs.acs.org/JPCC

Modeling Iron−Gold Nanoparticles Using a Dedicated Semi-Empirical Potential: Application to the Stability of Core−Shell Structures

F. Calvo,[†] N. Combe,[‡] J. Morillo,[‡] and M. Benoit*[,‡]

[†]University Grenoble Alpes and CNRS, LIPHY, F-38000 Grenoble, France

[‡]CEMES-CNRS, 29 rue Jeanne Marvig, 31055 Toulouse Cedex, France

Supporting Information

ABSTRACT: Core−shell nanoparticles made from iron embedded in gold have a strong potential interest in nanomedicine, the Au shell providing an efficient biocompatible coating for the magnetic Fe core. With the aim of determining theoretically the equilibrium morphologies of Fe−Au nanoparticles in a broad size range and with different compositions, a semiempirical many-body Fe−Au potential was designed combining well-established models for the pure metals and introducing dedicated contributions for the interactions involving mixed elements. The potential was parametrized against various energetic properties involving impurities, intermetallics, and finite clusters obtained using density functional calculations in the generalized gradient approximation. The potential was tested to investigate Fe−Au nanoparticles near equiconcentration containing about 1000−2000 atoms at finite temperature using parallel tempering Monte Carlo simulations initiated from the core−shell structure. The core−shell nanoparticles are found to be thermally stable up to about 800 K, at which point the gold outer layer starts to melt, with the iron core remaining stable up to approximately 1200 K. In contrast, the alternative potential developed by Zhou and co-workers (Zhou, X. Z.; Johnson, R. A.; Wadley, H. N. G. *Phys. Rev. B*, 2004, *69*, 144113) predicts a strong tendency for mixing, the core−shell structure appearing energetically metastable. The two models also predict significantly different vibrational spectra.

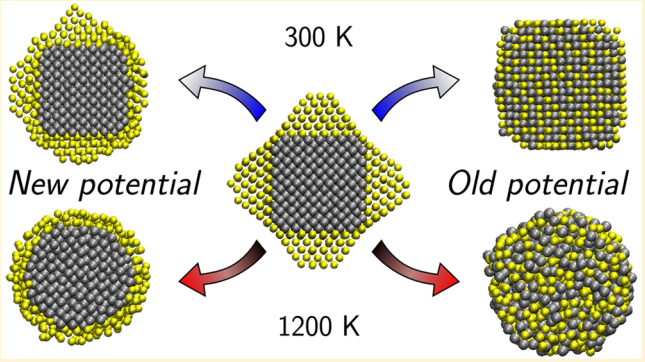

1. INTRODUCTION

The remarkable properties of nanoparticles (NPs) strongly depend on their morphology, whatever their field of applications. Beyond the size of the NPs, a precise control of their structure and shape is essential to master their physical properties as well as their interaction with the environment. To achieve this goal, a deep understanding of the formation mechanisms of NPs is essential. Unfortunately, owing to the often complex bulk phase diagram, to finite size effects, and to the interplay between thermodynamical and kinetic stabilities, predicting the morphology of nanoparticles containing thousands of atoms or more remains a highly complex and challenging issue for systems with two or more components. One morphology of particular applicative interest is the core−shell motif, which can lead to multifunctionality, generate entirely new properties that either of the two metals do not possess, and ensure the stabilization of specific external facets with desirable properties.[1−5]

While the equilibrium shape in sufficiently large monometallic nanocrystals can be predicted by the well-known Wulff construction theorem,[6] the shape of core−shell nanocrystals can rarely be anticipated.[7] In a previous work, Fe@Au nanocrystals with a peculiar morphology made of an iron nanocube coated by truncated gold pyramids could be synthesized by vapor phase sequential deposition.[8] Transmission electron microscopy analyses showed that the Au shell is actually epitaxially grown on the (100) facets of the iron cubic core. The remarkable stability of these Fe@Au NPs with a centered core was found to be preserved in an extended size range and was attributed to the low misfit at the Fe/Au(100) interface compared to other low miscible systems.[8−10] However, the stability of such highly symmetric structures remains unclear when the relative size of the shell with respect to the core varies significantly, with off-centered core−shell NPs becoming favorable in larger systems.[8]

Fe@Au core−shell NPs are very promising candidates for biomedical applications owing to the combination of a magnetic core and a biocompatible, chemically inert, and easily functionalized shell. Moreover, the Au shell provides an efficient coating for the toxic Fe core. Such NPs, with a pure Fe core, should be easier to manipulate (for drug delivery) or heat (for destroying tumors through hyperthermia) than their

Received: December 14, 2016
Revised: January 30, 2017
Published: February 3, 2017

DOI: 10.1021/acs.jpcc.6b12551
J. Phys. Chem. C 2017, 121, 4680−4691

oxides as well as provide enhanced contrast in magnetic resonance imaging.[11,12]

With the aim of determining theoretically the equilibrium morphologies of Fe−Au nanoparticles in a broad size range and with different compositions, methods with an explicit treatment of electronic structure are not affordable beyond a few thousands of atoms. Atomistic models, which are tractable up to millions of atoms, are necessary to properly describe the interatomic forces while allowing statistical or dynamical investigations over reasonably long or large scales. Semiempirical many-body potentials of the embedded-atom model (EAM) or second moment approximation (SMA) families are commonly used for metallic systems and often provide very satisfactory comparisons with experimental structural and thermodynamic properties.[13−15] Transition and noble metals that adopt a face centered crystal structure are usually the most convenient to model within the SMA approach; bcc metals are more complex and require more sophisticated functional forms to account for a greater number of parameters as well as additional but expensive angular-dependent corrections, in some cases. In the case of iron, accurate potentials have been developed covering both the crystalline phases and the disordered state by Mendelev and co-workers[16] and previously by Ackland et al.[17] and Dudarev et al.[18]

Except for similar metallic elements, a simple combination of the monometallic potential parameters is not sufficiently accurate to describe alloys, and parameters describing the interactions between unlike elements must be fitted to reproduce some alloying properties such as the heat of solution. Zhou and co-workers[19] developed an EAM potential database for 16 different metals that can be combined to generate directly the potentials to be used for the alloys. This was rendered possible by the use of a general functional form for the monometallic potentials that are normalized to a unique state.[19] To the best of our knowledge, the Fe−Au potential proposed by Zhou and co-workers is the only semiempirical potential available for these two metals together. So far, it has been used by Zientarsky and Chocyk,[20] who simulated multilayer bulk compounds and, very recently, by Hong and Rahman,[21] who used it to generate candidate structures for Fe−Au clusters to be refined at the level of density functional theory (DFT).

One severe issue explaining the limited amount of information regarding the Fe−Au system, especially from the experimental side, is that the two metals are generally not miscible. From the theoretical perspective, and as will be elaborated further below, ab initio calculations based on DFT also turn out to have many difficulties in describing properly both metals at the same time. Such difficulties, together with the potential importance of the Fe−Au system at the nanoscale, motivated us to look for an alternative semiempirical potential combining well-established models for the individual elements and a dedicated form for the mixed interactions parametrized on carefully evaluated DFT data. More specifically, we found that a suitable combination of properties evaluated from the different exchange and correlation (XC) functionals PBE[22] or PBEsol,[23] depending on which is the dominant element, provided more reliable data to be used in the training set. Among these properties, a greater attention was paid to the relative energies of various impurities in bulk or finite clusters, the formation energies of different intermetallic phases and, very importantly, to the interface energy responsible for the local stability at the (100) Fe−Au epitaxial contact.

In this article, we also present our first application of the potential to the fundamental stability at finite temperature of medium-size Fe−Au nanoparticles near the 50:50 composition and containing 1000−2000 atoms and assumed to reside in their core−shell geometry. Parallel tempering Monte Carlo simulations conducted with our potential are compared with similar calculations performed with the EAM potential by Zhou and co-workers.[19] We generally find that the core−shell morphology is metastable with both potentials, the core becoming slightly off-centered with our potential, while the Zhou EAM potential predicts the low energy structures to be random alloys. The two potentials were also tested on vibrational properties, the density of vibrational states appearing to depend also markedly on the underlying model and showing a significant dependence on chemical ordering within the nanoparticles.

The paper is organized as follows. In the next section, we describe the functional form chosen for our semiempirical potential and the electronic structure calculations performed to generate the training set. Application to the structural, thermodynamical, and vibrational properties of selected Fe−Au nanoparticles is presented in Section 3 before finally giving some concluding remarks in Section 4.

2. SEMIEMPIRICAL POTENTIAL FOR FE−AU

With the purpose of modeling bimetallic nanoparticles containing several thousands of atoms and to monitor their evolution over reasonable time scales and at finite temperature, we followed the approach of many-body semiempirical potentials which have a long-standing history in the computational description of metal nanoparticles.[15]

2.1. Functional Form. Accurate many-body potentials of the embedded-atom model family are available for both iron[16−18] and gold,[13,14,24] and we chose to base our own potential on two such models. We denote by $\mathbf{R} = \{\mathbf{r}_1,...,\mathbf{r}_N\} = (\mathbf{R}_{Fe},\mathbf{R}_{Au})$ the collective variables of positions of all N atoms, with $\mathbf{R}_X$ the set of positions of all elements of type X = Fe or Au. The total potential energy of the system is written as the generic EAM form

$$V(\mathbf{R}) = \sum_{i<j} V_{ij}(r_{ij}) + \sum_i F_i(\rho_i) \quad (1)$$

$$\rho_i = \sum_{j\neq i} \rho_{ij}(r_{ij}) \quad (2)$$

where we introduced the functions V_{ij} and ρ_{ij} that depend on the interatomic distance r_{ij} and the embedding functions F_i that depend on the local density ρ_i. All of these functions depend on the atom types and were chosen to match exactly some existing potentials for the pure metals. The complete expression is given as Supporting Information for sake of brevity.

Expressions for the terms $V_{FeFe}(r)$, $\rho_{FeFe}(r)$, and $F_{Fe}(\rho)$ were taken from Mendelev and co-workers,[16] whose potential is probably the most accurate model of this kind (i.e., without angular corrections) for iron in a broad range of thermodynamical conditions. For pure gold, the potential was chosen to match the second-moment approximation model reparametrized by Chamati and Papanicolaou[24] to improve the description of surface properties.

The form of the SMA potential, which involves only a limited number of parameters and well-behaved exponential forms, was adopted to represent the mixed Fe−Au terms of our potential:

DOI: 10.1021/acs.jpcc.6b12551
J. Phys. Chem. C 2017, 121, 4680−4691

Table 1. Lattice Parameters, Bulk Modulus, and (001) Surface Energies of Fe and Au Computed with Several Exchange and Correlation Functionals

	Fe			Au		
	a (Å)	B_0 (GPa)	γ_{001} (mJ/m^2)	a (Å)	B_0 (GPa)	γ_{001} (mJ/m^2)
PBE	2.835	186	2478	4.174	136	873
PBEsol	2.789	211	3035	4.098	174	1175
vdW-optB86b	2.807	199	3030	4.138	146	1268
exptl	2.866[a]	165[a]	2417[b]	4.08[c]	162−180[d]	1500[b]
		168[c]	2475[e]	4.079[ad]	167[a]	
		168−172[f]	2550[g]		180[h]	

[a]Ref 31. [b]Ref 32. [c]Ref 33. [d]Ref 34. [e]Ref 35. [f]Ref 36. [g]Ref 37. [h]Ref 38.

$$V_{\mathrm{FeAu}}(r) = 2E^0_{\mathrm{FeAu}}\exp\left[-p_{\mathrm{FeAu}}\left(\frac{r_{ij}}{r^0_{\mathrm{FeAu}}} - 1\right)\right] \quad (3)$$

$$\rho_{\mathrm{FeAu}}(r) = \xi^2_{\mathrm{FeAu}}\exp\left[-2q_{\mathrm{FeAu}}\left(\frac{r_{ij}}{r^0_{\mathrm{FeAu}}} - 1\right)\right] \quad (4)$$

$$\rho_{\mathrm{AuFe}}(r) = \xi^2_{\mathrm{AuFe}}\exp\left[-2q_{\mathrm{AuFe}}\left(\frac{r_{ij}}{r^0_{\mathrm{FeAu}}} - 1\right)\right] \quad (5)$$

where the last two terms ρ_{FeAu} and ρ_{AuFe} respectively denote the contributions of surrounding gold atoms to the electronic density of a specific iron atom and vice versa. Note that for V_{FeAu} we used the so-called effective pair format[25] in which the exponential is replaced by a Morse function but adding a term linear in the densities $-C_{\mathrm{Fe}}\rho_{\mathrm{FeAu}} - C_{\mathrm{Au}}\rho_{\mathrm{AuFe}}$, compensated exactly by removing this contribution from the embedding function, $F_i(\rho) \rightarrow F_i(\rho) + C_i\rho$. The two constants C_{Au} and C_{Fe} are chosen in such a way that the embedding function is minimum at the equilibrium density. These parameters are intrinsic to the pure metals and, for the two present potentials, are given by $C_{\mathrm{Fe}} = 0.114955$ eV and $C_{\mathrm{Au}} = 0.07963$ eV.

In the previous equations, we explicitly distinguished the contributions of gold to the local density of iron and vice versa by introducing unsymmetrical parameters ξ_{FeAu} and ξ_{AuFe} and q_{FeAu} and q_{AuFe}. However, only one distance parameter, r^0_{FeAu}, was used. For Fe−Au and Au−Au terms, all distance-dependent terms were also weighted by a fifth-order polynomial function smoothly cutting from 1 to 0 between the distances 7.05 and 7.65 Å, i.e., beyond the third neighbors.

2.2. Electronic Structure Calculations. To calibrate the semiempirical potential, DFT calculations were carried out for a variety of bulk and slab systems using the projector augmented wave (PAW) method,[26,27] as implemented in the VASP software package.[28−30] As mentioned in the introduction, we found significant difficulties in selecting an XC functional for Fe−Au mixed systems that is of similar accuracy for both pure elements. Table 1 gives the lattice parameter, bulk modulus, and (001) surface energies for iron and gold calculated using several functionals and compared with experimental measurements.

Apart from the well-known PBE functional,[22] we also tested the PBEsol functional, which was specially designed to improve equilibrium properties of densely packed solids and their surfaces.[23] Among the family of modern dispersion-corrected nonlocal functionals developed by Dion et al.,[39] often referred to as vdW-DF, the so-called optB86b functional optimized by Klimes et al.[40] was selected as well, owing to its ability to describe the structural properties of many solids.

Spin-polarized calculations were performed with a plane wave cutoff of 650 eV and a Methfessel−Paxton smearing parameter σ of 0.01 eV.[41] For bcc Fe and fcc Au bulk properties, a Monkhorst−Pack mesh of 20 × 20 × 20 and 12 × 12 × 12 k-points[42] were chosen, respectively. For surface calculations, the sizes of the slabs were chosen so that the interlayer distance in the center of the slab is the same as that of the bulk, as in previously published calculations.[43] A vacuum layer of at least 12 Å was introduced to avoid interactions between the periodic images, and the number of k-points in the direction perpendicular to the surface was reduced to 1.

The results of Table 1 show that none of the tested functionals is capable of describing properly the bulk and surface properties of Fe and Au simultaneously. The PBE functional gives very good agreement with experimental properties for Fe, whereas PBEsol better reproduces the experimental data for Au, the dispersion-corrected functional failing to solve the discrepancy. In view of these contrasted results, we found it more consistent to compute the properties of mixed Fe−Au compounds using both functionals: iron-rich and gold-rich systems were computed with the PBE and PBEsol functionals, respectively. For intermetallics with varying composition, weighted averages between the PBE and PBEsol data were used.

To parametrize the potential, the following energetic properties were calculated: (i) the dissolution energies of one atom in the other bulk metal, (ii) the alloying energies of selected intermetallic systems, (iii) the substitution energies of one atom in highly symmetric medium size clusters of the other metal, and (iv) the Au(001)/Fe(001) interface energy that is essential for describing core−shell Fe−Au NPs.

Dissolution energies were computed using the following formula:

$$\Delta E_{\mathrm{X,Y}} = E_{\mathrm{tot}}(\mathrm{XY}_{N-1}) - \frac{(N-1)}{N}E_{\mathrm{tot}}(\mathrm{Y}_N) - E^{\mathrm{bulk}}_{\mathrm{at}}(\mathrm{X}) \quad (6)$$

where X and Y stand for Fe or Au, $E_{\mathrm{tot}}(\mathrm{XY}_{N-1})$ is the total energy of the system with N Y atoms, in which one Y atom was substituted for X, $E_{\mathrm{tot}}(\mathrm{Y}_N)$ is the total energy of the system with N Y atoms, and $E^{\mathrm{bulk}}_{\mathrm{at}}(\mathrm{X})$ is the bulk energy per atom of the X metal. For the dissolution energy of Au in Fe, one Au atom was substituted for a Fe atom in a bcc crystal of 256 atoms. For the dissolution energy of Fe in Au, one Fe atom was substituted for a Au atom in an fcc crystal of 108 atoms. The Au-rich and Fe-rich systems were computed using the PBEsol and the PBE XC functionals, respectively, and the resulting DFT dissolution energies, after relaxation of the atomic positions and cell, are shown in Table 2. For such relatively small system sizes, the dissolution energies may not be fully converged due to the use

DOI: 10.1021/acs.jpcc.6b12551
J. Phys. Chem. C 2017, 121, 4680−4691

Table 2. Energies of the Various Systems in the Training Set at the DFT Level (Reference Values) Obtained from the Present EAM Potential or the Alternative Potential by Zhou and Coworkers[a]

system	DFT	present potential	Zhou et al.
Au in bcc Fe	1.040	0.984	−5.093
Fe in fcc Au	1.693	0.238	−5.100
$Fe_{0.25}Au_{0.75}$ as D_{03}	0.1324	0.828	−0.369
$Fe_{0.25}Au_{0.75}$ as L_{12}	0.1940	0.856	−0.361
$Fe_{0.5}Au_{0.5}$ as B_2	0.2553	0.955	−0.526
$Fe_{0.5}Au_{0.5}$ as L_{10}	0.1307	0.826	−0.517
$Fe_{0.75}Au_{0.25}$ as D_{03}	0.1983	0.618	−0.547
$Fe_{0.75}Au_{0.25}$ as L_{12}	0.0564	0.569	−0.532
$Au_{54}Fe$ (0)	0	0	0
$Au_{54}Fe$ (2.76)	1.417	1.394	0.760
$Au_{54}Fe$ (4.49)	2.616	0.984	1.598
$Au_{54}Fe$ (5.16)	1.263	0.504	1.538
$Fe_{64}Au$ (0)	1.614	1.193	−0.473
$Fe_{64}Au$ (2.50)	2.374	1.402	−0.434
$Fe_{64}Au$ (4.52)	0.802	0.774	−0.360
$Fe_{64}Au$ (5.12)	0	0	0
adhesion energy	2.694	2.694	3.110

[a]The relative cluster energies are identified by the distance of the impurity to the center in parentheses. All energies are in eV except the adhesion energy in J/m^2, and distances are in Å.

of periodic boundary conditions. However, assuming that size effects convey similarly for the semiempirical potential, these data can be used in the fit of the potential parameters provided that they are computed using the same system sizes.

Concerning alloying energies, the 6 following intermetallic structures based on the bcc or fcc lattices with 1:3, 1:1, and 3:1 compositions were considered, using the Strukturbericht notations: $Fe_{0.25}Au_{0.75}$ as D_{03} (bcc), $Fe_{0.25}Au_{0.75}$ as L_{12} (fcc), $Fe_{0.5}Au_{0.5}$ as B_2 (bcc), $Fe_{0.5}Au_{0.5}$ as L_{10} (fcc), $Fe_{0.75}Au_{0.25}$ as D_{03} (bcc), and $Fe_{0.75}Au_{0.25}$ as L_{12} (fcc). For all of these alloys, different magnetic states for iron were computed with only the lowest magnetic states being considered. In the more complex case of the D_{03} alloy, for which the unit cell is made of 16 atoms, only the ferromagnetic state was studied. The mixing energy E_{mix} was computed in such a way that[44]

$$E_{tot} = N_{Au}E_{Au}^{bulk} + N_{Fe}E_{Fe}^{bulk} + (N_{Au} + N_{Fe})E_{mix} \quad (7)$$

where E_{tot} is the total energy of the intermetallic system, E_X^{bulk} is the bulk atomic energy of metal X, and N_X is the number of X atoms in the system. This quantity was introduced for nanoalloys by Jellinek and Krissinel[44] as a suitable index for comparing systems with common size but different compositions. In the case of elements with a large size mismatch, it was suggested by Fortunelli and co-workers[45,46] to locally reoptimize all geometries before computing the mixing energies to remove the possibly large but physically less significant strain energy. For the present intermetallic compounds, atomic positions and cell parameters were relaxed simultaneously. For these calculations, both PBE and PBEsol functionals were used, and the resulting lattice parameters are presented in Figure 1 for the two considered crystalline structures.

For both lattices, the lattice parameters obtained with PBE are always larger than the PBEsol values. Because the PBE (respectively PBEsol) results are closer to experiment for Fe (respectively Au), we attempted to use weighted averages between the corresponding data to represent lattice parameters

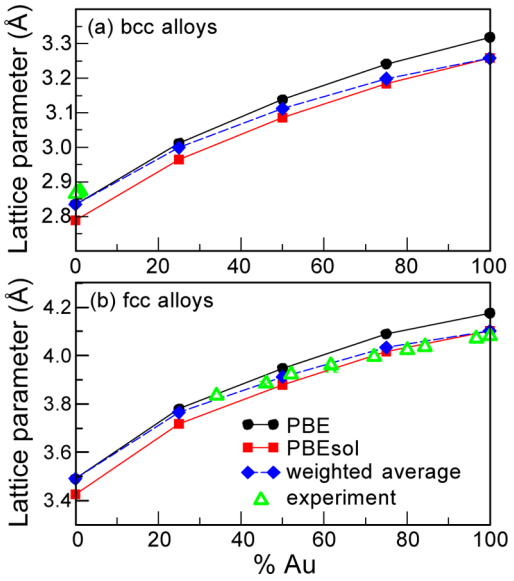

Figure 1. Variations of the lattice parameters of various intermetallic Fe−Au structures as a function of the gold concentration, as obtained with the PBE (black circles) and the PBEsol (red squares) functionals: (a) bcc lattices and (b) fcc lattices. The blue diamonds are weighted averages of the PBE and PBEsol data, and the green triangles are experimental data from Okamoto and co-workers.[47]

and mixing energies as close as possible to experimental data, the weights being simply taken as the concentration of the corresponding metal. The lattice parameters thus obtained, also shown in Figure 1, compare much better with the experimental measurements of Okamoto and co-workers.[47]

The mixing energies obtained for the same intermetallics are represented in Figure 2 again using the two XC functionals.

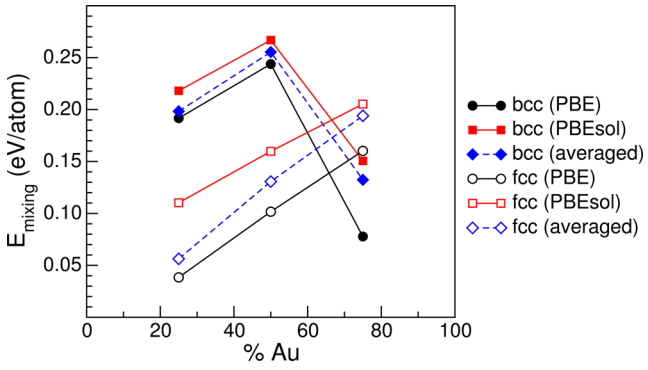

Figure 2. Mixing energies of intermetallic compounds with different crystal structures as a function of the gold concentration for the bcc (filled symbols) and fcc (open symbols) systems and as computed using the PBE (black symbols) and PBEsol (red symbols) exchange-correlation functionals. The blue diamonds are the corresponding weighted averages.

The weighted averages are also reported. For all studied systems, the mixing energies are strictly positive, which indicates the Fe−Au intermetallics are metastable, the two metals displaying a strong immiscible character. When the two crystal structures are compared, fcc alloys appear more stable than the bcc systems over a large range of compositions. However, the D_{03} (bcc) structure is more stable than L_{12} (fcc) at the $Fe_{0.25}Au_{0.75}$ composition. Experimentally, fcc solid

DOI: 10.1021/acs.jpcc.6b12551
J. Phys. Chem. C 2017, 121, 4680−4691

solutions are obtained for gold concentrations higher than 33% (ref 47) and, for Fe content higher than 92%, structures based on γ-Fe seem to be more favorable than those based on α-Fe (ref 47). Our result for the 1:3 composition cannot be directly compared with experiments, which exhibit disordered solid solutions at high temperature rather than order intermetallics at 0 K. In view of the fundamental difficulties of DFT to treat both metals simultaneously, it would be useful to explore other, perhaps less phenomenological, ways of accounting for the presence of both metals when describing intermetallics.

To better capture size-dependent properties that are an essential feature of nanoparticles, substitution energies of unlike atoms in medium-size clusters were also computed, again employing PBE and PBEsol for Au- and Fe-rich systems, respectively. The systems chosen are the icosahedral Au_{55} cluster, only exposing (111) fcc facets (I_h point group), and the two-layer bcc Fe_{65} cluster extracted from the periodic crystal (O_h point group). For each cluster, four substitutional sites k can be distinguished, and we considered the energies $\Delta E_k = E_k - E_k^{\min}$ of each isomer relative to the most stable of its kind: for $Au_{54}Fe$, the lowest substitutional site for iron is at the icosahedron center; for $Fe_{64}Au$, the optimal site for gold is at the vertex. The resulting DFT substitution energies are shown in Table 2.

Finally, to ensure that the epitaxial relationship between Au(001) and Fe(001) at 45° is favorable, we introduced the interface energy Au(001)/Fe(001) in the training set of our potential. This introduction is motivated by our earlier observation[8] that the stability of Fe@Au core−shell NPs elaborated by vapor deposition is due to the favorable epitaxial relationship on the cube facets between Fe(001) and Au(001) at 45°. This interface energy was determined previously using DFT carried with the PBE functional.[43,48] In the present case, the poor performance of the PBE functional for gold in the lattice parameter and (001) surface energy relative to experimental data results in a mismatch at the interface of 4.11%, at significant variance with the measured value of only 0.66% (ref 43). We showed in ref 43 that, for a large part, this discrepancy does not affect the computed value of the interface energy, except for a term representing the interface stress.

It is possible to relate the interface energy to the work of adhesion of a Au(001) slab on an Fe(001) slab, W_{adh}, which can be evaluated in a straightforward way from total energy DFT calculations, following:

$$W_{adh} = \frac{(E_{Fe} + E_{Au} - E_{Fe/Au})}{A} \quad (8)$$

where E_{Fe} and E_{Au} are the total energies of the bare Fe and Au slabs, respectively, $E_{Fe/Au}$ being the total energy of the interface system, and A is the area of the interface. The work of adhesion is related to the interface energy γ_{int} through the equation

$$W_{adh} = \gamma_{(001)}^{Fe} + \gamma_{(001)}^{Au} + 2\sigma_{(001)}^{Au}\epsilon_{xx} - (\gamma_{int} + 2\sigma_{int}\epsilon_{xx}) \quad (9)$$

where $\gamma_{(001)}^{X}$ is the surface energy of X(001), $\sigma_{(001)}^{Au}$ is the Au surface stress, σ_{int} is the interface stress, and ϵ_{xx} is the in-plane strain due to the lattice mismatch. From earlier DFT calculations,[48] the work of adhesion is evaluated as 2.85 J/m^2, which leads to an interface energy of 0.376 J/m^2, taking into account the interface and surface stress terms for the PBE lattice mismatch.

The chosen semiempirical potentials for Fe and for Au reproduce the experimental mismatch to a very good accuracy. This leads to a very low misfit at the Au(001)/Fe(001) interface that allows the interface and surface stress terms to be neglected in the expression for the work of adhesion in a first approximation. The EAM potential of Mendelev[16] gives a Fe(001) surface energy of 2.009 J/m^2, and the SMA potential of Chamati[24] gives a Au(001) surface energy of 1.061 J/m^2. When the interface energy is fixed to the DFT value of 0.376 J/m^2, the resulting work of adhesion that should be satisfied by the model is therefore equal to 2.694 J/m^2.

2.3. Parametrization and Model Assessment. The present potential is aimed to describe nanoscale systems in which the proportion of surface and interface atoms is important. We adjusted the 7 parameters of the Fe−Au contribution to the potential by best reproducing the above-described 15 data items whose reference values were provided by the DFT calculations: 2 bulk substitution energies, 6 intermetallic energies, 2 × 3 cluster energies, and 1 adhesion energy. An error function containing the above 15 contributions was minimized by performing various series of zero-temperature Monte Carlo simulations in parameter space, slowly reducing the maximum displacement amplitude by 3/4 every 1000 MC cycles. In the error function, a 10-fold weight was given to the interface adhesion energy.

The final values obtained for these 15 properties are reported in Table 2 and compared to the predictions of the alternative EAM potential by Zhou and co-workers.[19] The optimal parameters themselves are p_{FeAu} = 2.8203, q_{FeAu} = 1.6334, q_{AuFe} = 2.7193, E^0_{FeAu} = 0.021155 eV, ξ_{FeAu} = 0.082649 eV, ξ_{AuFe} = 0.016565 eV, and r^0_{FeAu} = 3.5128 Å.

Clearly, our EAM potential is not able to reproduce all of the required properties in the training set with the same high accuracy. In particular, it performs better on gold impurities inside iron in either cluster or bulk phases than on the reverse case of iron inside gold. It is also worth noting that the corresponding DFT value of 1.693 eV is very high and hard to reconcile with the experimentally known low transition temperature to the solid solution in gold-rich alloys.[47,49] This observation suggests that electronic and vibrational entropies and the internal energy should contribute significantly to the free energy of the solid solution. The intermetallics are also not perfectly described, although it should be emphasized that no experimental data are available for these structures. Yet, they are all locally stable with both potentials, suggesting that the intermetallics are also metastable structures within the DFT descriptions. However, the most striking feature is the very different behavior of the EAM potential by Zhou et al. which, despite a reasonable adhesion energy at the gold/iron interface, exhibits a strong tendency for mixing, as seen from the systematically negative substitution energies and mixing energies for all intermetallic phases. The tendency for alloying is also manifested in the different ordering among the isomers of the gold-substituted Fe_{65} clusters with gold preferring the central position in the Zhou EAM potential. This result is in contradiction with both the DFT and present EAM data and should lead to contrasted behaviors in larger NPs. We tried to reoptimize the mixed Fe−Au parameters of the Zhou EAM potential, keeping all original contributions for Fe−Fe and Au−Au unchanged, but could not successfully cure this tendency for mixing.

3. APPLICATION TO FE@AU NANOPARTICLES

The newly parametrized EAM potential for Fe−Au was first tested to evaluate the stable morphologies, thermal equilibrium,

DOI: 10.1021/acs.jpcc.6b12551
J. Phys. Chem. C 2017, 121, 4680−4691

and vibrational properties of medium-sized nanoparticles containing about 1000−2000 atoms. Two nanoparticles (one of ≈1000 atoms and one of ≈2000 atoms) were initially constructed by first building a bcc Fe cube with truncated edges. Six truncated gold pyramids with height parallel to the (001) crystallographic direction were then placed on the 6 cube facets following the Au(001)/Fe(001) epitaxial relationship at 45°. The pyramid bases were chosen large enough to cover the truncated edges of the Fe cubes. After a conjugated gradient relaxation using the present EAM potential, excess Au rows between the gold pyramids at the cube edges could be observed. These excess rows were then removed, and the structure was relaxed again. The two initial NPs generated this way were then $Fe_{491}Au_{516}$ and $Fe_{1149}Au_{1194}$.

3.1. Computational Protocol. Parallel tempering[50,51] Monte Carlo simulations were performed for both nanoparticles in the 300−1500 K temperature range using initially a geometrically distributed temperature ladder with 32 rungs and adjusting some rungs near the phase transition to improve the exchange probabilities.[52−54] Individual Monte Carlo moves consisted of random individual displacements (90%) and particle swaps between gold and iron atoms (10%). Exchanges between random pairs of neighboring replicas were attempted once every 10 MC cycles, one cycle representing N individual moves with N the total number of atoms. In the present work, 10 successive series 10^7 MC cycles were performed for each system at each temperature.

The parallel tempering strategy was chosen as one of the practical and efficient ways to overcome broken ergodicity in simulation and in particular for its ability to achieve broad sampling of the energy landscapes and locate low-energy structures. While this approach should enable a satisfactory description of the equilibrium properties in the canonical ensemble, a second series of Monte Carlo simulations was performed to investigate the core−shell metastability by discarding the exchanges between replicas, thus mimicking the natural behavior of the nanoparticle under imposed heating.

From the Monte Carlo simulations, the internal energy $U = \langle E \rangle$ and various structural properties were obtained using a weighted histogram analysis method.[55,56] Here, we considered a global mixing parameter $\langle \mu \rangle$ where the configuration-dependent μ is defined from the local connectivity of individual atoms as[57]

$$\mu = \frac{N_{FeFe} + N_{AuAu} - N_{FeAu}}{N_{FeFe} + N_{AuAu} + N_{FeAu}} \tag{10}$$

where N_{AB} denotes the number of A−B bonds between first neighbors. The parameter μ displays high positive values for phase segregated systems but negative values for alloyed structures. Here, all bonds within 3.5 Å were considered to calculate μ.

In addition to the equilibrium structural and thermodynamical properties, we considered the vibrational response of the nanoparticles as a possible probe of their structure. In practice, 1000 configurations sampled at 300 K from the Monte Carlo simulations were locally minimized into as many inherent structures, and for each structure, a harmonic analysis was performed, giving a series of $3N - 6$ frequencies ω_i with associated normalized eigenvectors $\mathbf{U}_{ik}$, $k = 1,...,3N$. The vibrational density of states (VDOS) was then obtained by summing over the 1000 independent spectra. The specific contributions of gold and iron to the VDOS were also calculated by determining for each frequency ω_i the relative weights $c_{i,X}$ of individual elements X = Fe or Au:

$$c_{i,X} = \sum_k \delta_{kX} U_{ik}^2 \tag{11}$$

where δ_{kX} acts as a Kronecker symbol, taking the value 1 if atom k is of type X and 0 otherwise.

3.2. Thermodynamical Equilibrium. The variations of the internal energy of the two nanoparticles with increasing temperature, as predicted by the presently parametrized potential, are represented in Figure 3. A few representative snapshots showing the evolution of the representative NP morphologies, identified by labels i−iii and I−III, are depicted in Figure 4 after removing the front half for better visualization. For both particles, the internal energy shows smoothly increasing variations with a rather broad jump near 1200 K for the smaller NP and between 1000−1300 K for the larger NP. These stronger jumps are associated with finite size phase transitions[58] and will be discussed in more detail below.

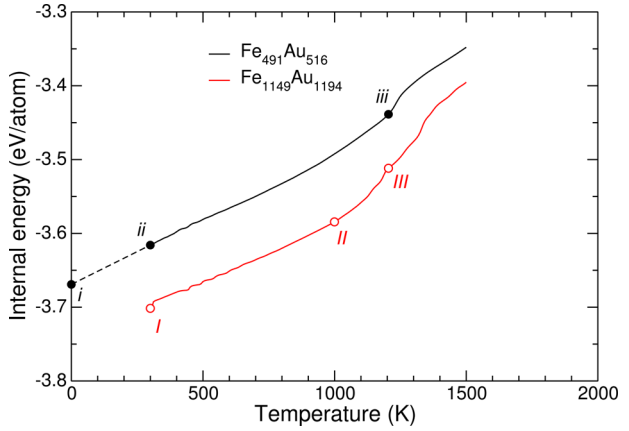

Figure 3. Internal energy obtained for the $Fe_{491}Au_{516}$ and $Fe_{1149}Au_{1194}$ nanoparticles as a function of temperature using the present EAM potential. Representative structures obtained at selected temperatures are identified by symbols and lowercase or uppercase letters and depicted in Figure 4. Structure i is the putative global minimum of the smallest NP at 0 K.

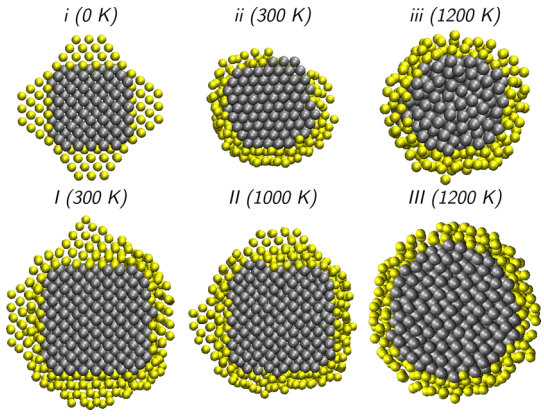

Figure 4. Half-cut structures of $Fe_{491}Au_{516}$ and $Fe_{1149}Au_{1194}$ at various temperatures, corresponding to the labels i−iii and I−III in Figure 3, as obtained from parallel tempering Monte Carlo simulations with the present EAM potential.

DOI: 10.1021/acs.jpcc.6b12551
J. Phys. Chem. C 2017, 121, 4680−4691

The first remarkable result obtained from these simulations is the thermal stability of the initial core−shell structures, even though the initial, highly symmetric (octahedral) geometries are not lowest in energy. The parallel tempering MC simulations manage to locate slightly more stable structures in which the iron core remains essentially unchanged but the gold shells undergo some rearrangements to better accommodate the epitaxial contact. In the smaller NP, the lowest-energy structure (Figure 4i) can barely be distinguished from the octahedral initial condition, above which it lies by only 8 meV/atom. In the larger NP, the rearrangement is more significant, with a distinct symmetry breaking occurring with a portion of the outer gold atoms moving to the other sides and the iron core appearing moderately off-centered. This rearrangement can be more clearly seen at 300 K (Figure 4I), but at this temperature, the fluxional motion of the gold shell can also clearly be seen for the smaller NP, where a transition to an off-centered Janus-type structure takes place with the iron core partly protruding through the gold shell (Figure 4ii). In the larger NP, a slight tendency to protrusion is also noticed above 800 K (Figure 4II), but the core remains completely covered by gold.

The increase in internal energies above approximately 1200 K signals the melting phase change,[58] in which the gold atoms isotropically coat the molten iron core (Figures 4iii and III). Even in their liquid state, both iron−gold nanoparticles thus remain well phase separated within the core−shell chemical ordering. At even higher temperature, the NPs would dissociate had they not be kept connected by a container. The dissociation proceeds by dipolar elongation (results not shown).

Parallel tempering MC simulations were also performed using the Zhou EAM potential, again starting from the same core−shell structures as with the previous simulations. The variations of internal energy with increasing temperature have been reported in Figure 5, and representative pictures of the particles extracted from the simulations at different temperatures are shown in Figure 6. The possibility of swapping atoms of different types and to exchange configurations between neighboring trajectories produces much more stable minima that are based on the face-centered cubic crystal but with a clear random alloy character; they are shown in Figures 6b and B. The internal energies exhibit rather strong signatures of phase changes at about 1100 K for the smaller nanoparticle and at 1200−1300 K for the larger NP. Inspection of the structures reveals that both nanoparticles melt as whole, the crystalline order being lost, but chemical disorder present in the low-temperature phase remaining above the melting range (Figures 6c and C). At very high temperatures, both molten particles display again dipolar deformations on their way to dissociation.

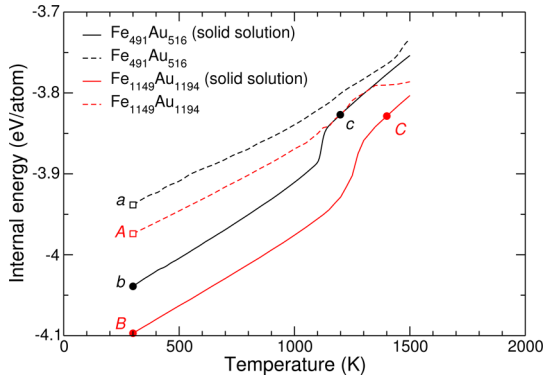

Figure 5. The information presented is the same as that in Figure 3 but obtained using the EAM potential by Zhou and co-workers. Two series of results are shown, as produced from parallel tempering (full lines) or conventional (dashed lines) Monte Carlo simulations. In the latter case, the simulations are initiated from the core−shell structure. Representative structures obtained at selected temperatures are identified by symbols and lowercase or uppercase letters and depicted in Figure 6.

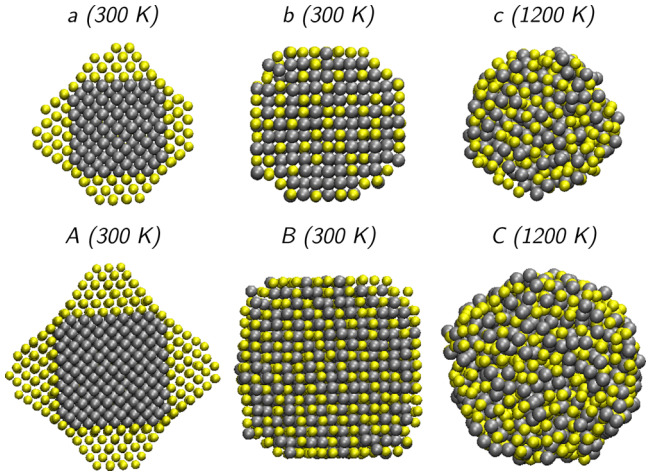

Figure 6. Typical structures of $Fe_{491}Au_{516}$ and $Fe_{1149}Au_{1194}$ at various temperatures, corresponding to the labels a−c and A−C in Figure 5, as obtained from parallel tempering Monte Carlo simulations with the EAM potential of Zhou and co-workers.

The solid solution behavior obtained here for the EAM model by Zhou et al. is not surprising in light of the tendency for mixing already noted in the previous section. This behavior is a priori inconsistent with experiment, in which aging of nanoparticles synthesized in a core−shell fashion would naturally produce alloyed structures should they be the most stable. Although the present work does not directly address the kinetics of such transformations,[59] the Zhou EAM potential thus appears probably unrealistic to describe core−shell nanoparticles.

With this limitation in mind, we tried to circumvent the metastability issue by repeating the Monte Carlo simulations but discarding exchange moves between replicas and not allowing any swapping move between unlike atoms. This procedure makes the computational methodology similar to more conventional stochastic molecular dynamics trajectories and manages to keep a better track of the initial conditions imposed to the simulations. The final structures obtained at 300 K for both NPs, shown in Figures 6a and A, remained very close to the initially symmetric structures with truncated gold pyramids coating the cubic iron core.

The internal energies obtained using this nonergodic simulation protocol, also represented in Figure 5, show contrasted results with respect to the parallel tempering MC simulations with the initial core−shell structures appearing much higher in energy than the random alloys located with the latter method. Under such constraints, the internal energies of the two NPs vary much more smoothly and do not exhibit phase changes as strong as when they are left to adopt their more stable solid solution form. However, at high temperatures, they eventually melt and mix nearly simultaneously, the

DOI: 10.1021/acs.jpcc.6b12551
J. Phys. Chem. C 2017, 121, 4680−4691

differences in internal energy with the ergodic solid solution results being now much lower.

Further considerations can be made about the phase diagram which, for the iron−gold sample, does not show compounds besides demixed phases at low temperature and solid solutions at high temperature in the gold-rich region.[47,49] From the dissolution energies $\Delta E_{Fe,Au}$ and $\Delta E_{Au,Fe}$, the transition temperatures $T_c(x)$ in the composition−temperature diagram above which the solid solution becomes more stable can be roughly evaluated in the limits $x_{Au} \to 0$ and $x_{Fe} \to 0$ as $x_c = \exp(-\Delta E/k_B T_c)$. Use of the values from Table 2 yields $T_c \simeq 350°$ for 1% iron in gold, which is in reasonable agreement with experimental data. In the iron-rich region, we get $T_c = 1450°$ for 0.1% gold in iron, which is noticeably higher than the experimental value, although of comparable magnitude.

Beyond these simple arguments, additional Monte Carlo simulations were performed under periodic boundary conditions starting from the intermetallic structures already employed to fit the potential. These simulations were carried out at constant zero pressure with possible swap moves between unlike atoms at the three same compositions of $Fe_{0.25}Au_{0.75}$, $Fe_{0.50}Au_{0.50}$, and $Fe_{0.75}Au_{0.25}$ starting from the fcc- or bcc-based intermetallics listed in Table 2. Our aim here is not to characterize the entire phase diagram of the Fe−Au system but only to obtain some insight into the fundamental properties of the present EAM potentials. The tendencies for unmixing and full mixing of the present potential and the Zhou EAM model, respectively, generally remain as such under periodic boundary conditions for these specific systems, as shown in Figure 7, where typical structures obtained at 300 K are depicted.

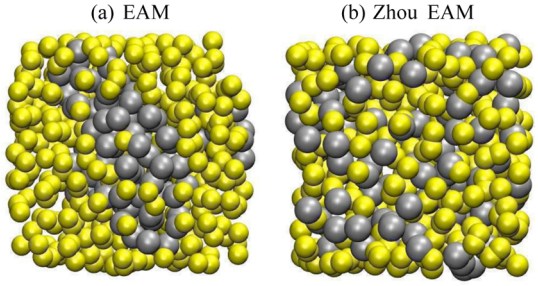

Figure 7. Configurations obtained from zero-pressure Monte Carlo simulations at T = 300 K with periodic boundaries and initiated from the L_{12} intermetallic $Fe_{25}Au_{0.75}$ using (a) the presently parametrized EAM potential and (b) the Zhou EAM potential. Iron and gold atoms are depicted as gray and yellow balls, respectively.

No clear evidence was found from similar simulations performed at higher temperatures for solid solution behavior in the gold-rich region. This is in agreement with the results obtained above on nanoparticles that remain phase separated up to the melting point. While such a feature could of course point out some intrinsic inaccuracy of the present potential at high temperature (fitted on static properties only), these complementary calculations confirm that, at least under ambient conditions, it is more realistic than the Zhou EAM potential for describing bulk compounds.

3.3. Chemical Ordering and Interface Structure. To shed more light on the stability of the core−shell configuration, and in particular how unlike elements are arranged relative to each other, we considered the structural order parameter provided by the average mixing index $\langle\mu\rangle$. The variations of this quantity with increasing temperature are represented in Figure 8 for the two nanoparticles in the three models, namely, the

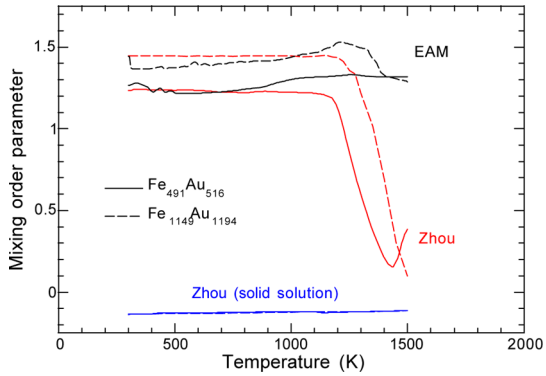

Figure 8. Average mixing order parameter $\langle\mu\rangle$ obtained for the $Fe_{491}Au_{516}$ (full lines) and $Fe_{1149}Au_{1194}$ (dashed lines) nanoparticles. The parallel tempering Monte Carlo results from the present EAM, and Zhou EAM potentials are shown in black and blue, respectively. The results obtained for the Zhou EAM potential using conventional Monte Carlo simulations initiated from the core−shell structure are shown in red.

presently parametrized EAM potential and the EAM potential by Zhou et al. simulated either ergodically or imposing the initially metastable core−shell initial structure.

The two metals remain phase separated with the present EAM potential even above the melting range, the mixing index displaying always positive values, and only minor but visible increases as the NPs melt. Conversely, the mixing order parameter for the Zhou EAM potential simulated with exchanges and particle swap unsurprisingly displays negative values that are essentially constant in the entire temperature range, the particles keeping a fully mixed character through the melting phase change. If the simulations are performed on the metastable core−shell structure, phase separation remains until about 1200 K for the smaller NP, 1300 K for the larger NP, and mixing sets in as the particles melt.

We also considered the mixing energy E_{mix} from eq 7 as a probe of the relative stability of the various configurations explored by the two potentials. For nanoparticles, the terms E_X^{bulk} should be replaced by the energies of the nanoparticles of the pure corresponding element at the geometry of the mixed NP, or as advocated by Fortunelli and co-workers[45,46] for such size-mismatched systems, after local reoptimization. Here, we calculated the mixing energies of the low-energy structures depicted in Figures 4 and 6, and the resulting values are reported in Table 3.

In the absence of relaxation, the mixing energy exhibits particularly low negative values for the core−shell structures with the presently introduced potential, much lower than that with the EAM potential of Zhou and co-workers. However, inspection of the static energies E_{Au} and E_{Fe} for the unrelaxed homogeneous structures of the mixed NP shows positive values, indicating that they are indeed quite far away from their equilibrium geometry and making the mixing energy even more negative. When this artifact is removed by geometry minimization, the overall picture shows opposite trends with the mixing energies associated with present potential being still negative but with a very low magnitude, while the Zhou EAM potential keeps markedly negative values. For both models, the

DOI: 10.1021/acs.jpcc.6b12551
J. Phys. Chem. C 2017, 121, 4680−4691

Table 3. Mixing Energies (E_{mix}) Obtained for Low-Energy Structures Labelled in Figures 4 and 6 with the Corresponding Potential[a]

structure and model	E_{mix} (eV/atom)	E_{mix} (eV/atom, relaxed)
i	−2.27	−0.019
ii	−2.50	−0.026
I	−2.43	−0.0091
II	−1.87	−0.034
a	−1.04	−0.27
b	−0.94	−0.37
A	−1.04	−0.25
B	−0.95	−0.38

[a]Values before and after geometry relaxation of the homogeneous clusters are given for E_{mix}.

mixing energies further decrease with the NPs finding more stable configurations (i → ii and I → II, *a* → *b* and *A* → *B*).

The local structure of the gold−iron interface in the two nanoparticles was also investigated by determining the pair distribution function $g(r_{FeAu})$, which gives the probability of finding Fe and Au atoms at distance r_{FeAu} from one another. The variations of these distributions calculated at 300 K with increasing radial distance are represented in Figure 9 for the

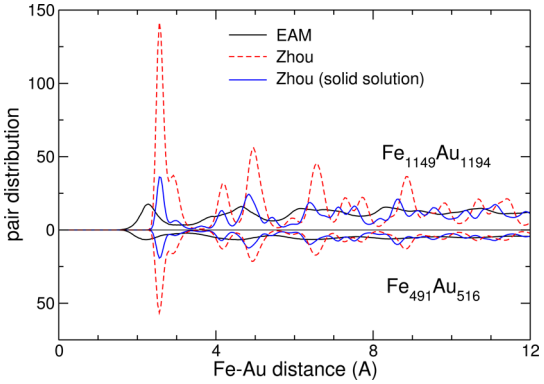

Figure 9. Pair distribution function $g(r_{FeAu})$ between iron and gold atoms obtained at 300 K for the $Fe_{491}Au_{516}$ (lower panel) and $Fe_{1149}Au_{1194}$ (upper panel) nanoparticles using parallel tempering Monte Carlo simulations with the present EAM and Zhou EAM potentials and conventional simulations for the Zhou EAM potential initiated from the core−shell structure.

two EAM models. As seen previously, the results obtained from the EAM potential by Zhou and co-workers but imposing the core−shell metastable struture are also reported. The gold−iron interface in the core−shell nanoparticles appears much less structured with the present EAM potential than when described with the Zhou EAM potential, already at short distances. This points to the much stronger Fe−Au bond in the latter model, also favoring mixing in absence of any restraint in the simulation. In particular, the Fe−Au distance is shorter with our potential, and the broader distribution of nearest-neighbors is consistent with the clearly nonsymmetric core−shell structure (ii) depicted in Figure 4. Letting now the NPs evolve as solid solutions leads to marked differences beyond the first neighbor distances $r > 4$ Å. Finally, no significant finite size effect can be noticed for the three simulations, the pair distributions scaling linearly with the nanoparticle size.

3.4. Vibrational Properties. Another way of characterizing the nanoparticles that has become increasingly accurate in recent years relies on their spectroscopic response in the optical range relevant to plasmonics[60,61] but also in the infrared range through nonlinear Raman[62,63] or pump−probe[64] measurements. In Figure 10, we show the densities of vibrational states

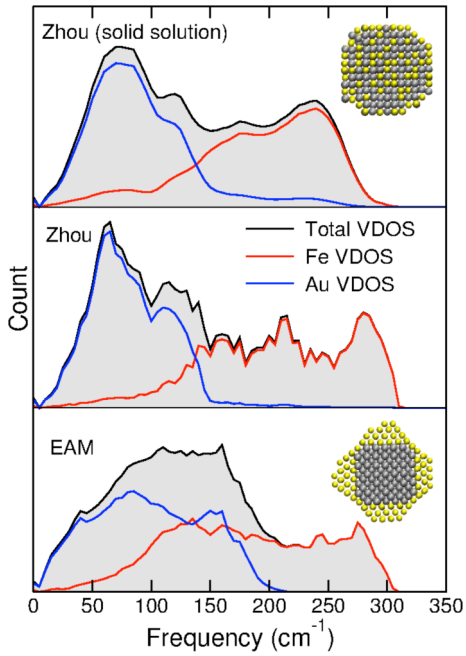

Figure 10. Vibrational densities of states obtained for a 300 K sample of 1000 configurations of the $Fe_{491}Au_{516}$ nanoparticle described using the present EAM potential (lower panel) and the Zhou EAM potential (upper panel), emphasizing the separate contributions of iron and gold atoms in red and blue, respectively. In the case of the Zhou EAM potential, the results are also shown for a sample originating from conventional simulations based on the core−shell structure (middle panel).

obtained for the smaller nanoparticle using the 300 K sample produced by the Monte Carlo simulations for the two potentials and, in the case of the Zhou EAM potential, imposing the core−shell structure or letting it evolve into a solid solution. For each spectrum, the specific contributions of gold and iron are indicated, as calculated using eq 11. All spectra show two main peaks corresponding to the vibrations of gold and iron atoms at lower and higher frequencies, respectively, consistently with their different masses. The two spectra calculated for core−shell structures predict a high frequency peak near 275 cm^{-1}, which is absent in the randomly alloyed nanoparticle. This feature is robust and does not depend significantly on the potential. However, the contribution for gold is quite different with a main peak near 60 cm^{-1} with the Zhou EAM potential but a much broader peak extending over 100−150 cm^{-1} with the presently parametrized potential. In this region, the vibrational modes are also much more mixed between gold and iron. The Zhou EAM potential also predicts relatively minor alloying effects with the gold peak near 60 cm^{-1} and the secondary peak near 110 cm^{-1} being preserved in the solid solution NP.

4. CONCLUDING REMARKS

The core−shell chemical ordering in bimetallic nanoparticles is of utmost interest for applications in which the physically relevant core is likely to react with the surrounding medium,

DOI: 10.1021/acs.jpcc.6b12551
J. Phys. Chem. C 2017, 121, 4680−4691

hence the need for protecting it by a more inert shell. It is also susceptible to lead to multifunctionality and generate new properties, e.g., in catalysis or optoelectronics. Understanding the formation mechanisms and stability of core−shell nanoparticles is a prerequisite for improving control over their properties. In the present contribution, we addressed the specific case of iron−gold nanoparticles, which could have valuable biomedical applications,[11,12] by means of computational modeling at the atomistic level of detail. In view of the reasonably large systems we aim to study, we chose the approach of semiempirical many-body potentials which have a long and successful history in the field of metal alloys. However, the only existing potential that we are aware of[19] turns out to be disputable in the absence of specific adjustment on experimental data for the nonmiscible Fe−Au system. Therefore, we carried out extensive density functional theory calculations of various bulk and finite size Fe−Au clusters and found it very difficult to correctly describe these compounds with a single exchange-correlation functional. The properties of the alloys turn out to be better represented by suitable averages over results obtained with either the PBE or the PBEsol functionals that are more appropriate for iron and gold, respectively.

The electronic structure data could be used to train a semiempirical potential of the EAM family, combining many-body potentials already available for iron[16] and gold[24] and adjusting only the mixed interaction, paying particular attention in the fitting process to the interface energy at the epitaxial Au(001)/Fe(001) contact at 45°. As a first application, the present potential was used to evaluate the intrinsic thermal stability of Fe@Au nanoparticles containing about 1000−2000 atoms near the 50% composition, performing Monte Carlo simulations possibly enhanced with parallel tempering to expand sampling of the energy landscape. We found the core−shell NPs to be thermally stable over a broad temperature range extending up to 1000 K or more even though the gold shell undergoes deformations already at room temperature to achieve more favorable off-centered morphologies with a less ordered interface structure with the iron core. In a recent finite-element modeling analysis of the same system,[8] although for much larger NPs than those presently considered, it has been shown that the morphology with a centered core was largely attributable to the low misfit at the Fe/Au(100) interface and to the prominent importance of surface energies. However, in this study, only perfect Fe cubes were considered, and the highly strained Au/Fe interface at the truncated Fe cube edges and corners was not taken into account. The off-centered morphologies obtained here might therefore be induced by strain relaxations at the cube edges. The role of strain relaxation on the optimal location of the iron core within the NP will be scrutinized in more detail in the future, notably considering the contribution of internal stress.[9]

In contrast, the EAM potential by Zhou and co-workers[19] predicts randomly mixed nanoparticles already at low temperatures and a mestatable core−shell structure when particle exchanges are forbidden. The two potentials also predict qualitatively different vibrational properties that reflect markedly different Fe−Au interactions.

Our potential is thus more realistic than the Zhou EAM potential at low temperatures, yet it cannot reproduce the solid solution behavior known in the experimental phase diagram for gold-rich compounds at high temperatures. Further refinements such as the inclusion of angular terms[65] or many-body screening functions[66] could be also added to the Fe−Au contributions that allow for more flexibility and transferability with the price of extending the training set. To assess the accuracy of our potential further, it would be useful to perform electron microscopy measurements on aging samples to determine whether a tendency for mixing is found over long times. It would also be of interest to explore the vibrational properties experimentally, e.g., by Raman spectroscopy, to discriminate between the respective contributions of the two metals.

However, our main perspective will be to exploit the potential to address the more complex problem of the formation mechanisms of the core−shell Fe@au nanoparticles in close relation with experiments,[8] working either at variable Fe/Au concentration in the semigrand canonical ensemble or addressing more directly the deposition process on a preformed core. Progress along these lines is expected in the near future.

■ ASSOCIATED CONTENT

Supporting Information

The Supporting Information is available free of charge on the ACS Publications website at DOI: 10.1021/acs.jpcc.6b12551.

Full expression and parameters of the EAM potential (PDF)

■ AUTHOR INFORMATION

Corresponding Author

*E-mail: magali.benoit@cemes.fr.

ORCID

F. Calvo: 0000-0002-3621-3046

Notes

The authors declare no competing financial interest.

■ ACKNOWLEDGMENTS

Financial support from GDR 3182 Nanoalliages is gratefully acknowledged. We also thank the regional computing center CALMIP for providing generous computational resources (Project p1141).

■ REFERENCES

(1) Cao, Y.; Jin, R.; Mirkin, C. DNA-Modified Core-Shell Ag/Au Nanoparticles. *J. Am. Chem. Soc.* **2001**, *123*, 7961−7962.

(2) Sao-Joao, S.; Giorgio, S.; Penisson, J. M.; Chapon, C.; Bourgeois, S.; Henry, C. Structure and Deformations of Pd-Ni Core-Shell Nanoparticles. *J. Phys. Chem. B* **2005**, *109*, 342−347.

(3) Cazayous, M.; Langlois, C.; Oikawa, T.; Ricolleau, C.; Sacuto, A. Cu-Ag Core-Shell Nanoparticles: A Direct Correlation Between Micro-Raman and Electron Microscopy. *Phys. Rev. B: Condens. Matter Mater. Phys.* **2006**, *73*, 113402.

(4) Sun, Q.; Kandalam, A.; Wang, Q.; Jena, P.; Kawazoe, Y.; Marquez, M. Effect of Au Coating on the Magnetic and Structural Properties of Fe Nanoclusters for Use in Biomedical Applications: A density functional Theory Study. *Phys. Rev. B: Condens. Matter Mater. Phys.* **2006**, *73*, 134409.

(5) Bao, Y.; Calderon, H.; Krishnan, K. Synthesis and Characterization of Magnetic-Optical Co-Au Core-Shell Nanoparticles. *J. Phys. Chem. C* **2007**, *111*, 1941−1944.

(6) Wulff, G. Zur Frage der Geschwindigkeit des Wachstums und der Auflösung der Krystallflächen. *Z. Kristallogr. - Cryst. Mater.* **1901**, *34*, 449−530.

(7) Ringe, E.; Van Duyne, R. P.; Marks, L. D. Wulff Construction for Alloy Nanoparticles. *Nano Lett.* **2011**, *11*, 3399−3403.

DOI: 10.1021/acs.jpcc.6b12551
J. Phys. Chem. C 2017, 121, 4680−4691

(8) Langlois, C.; Benzo, P.; Arenal, R.; Benoit, M.; Nicolai, J.; Combe, N.; Ponchet, A.; Casanove, M.-J. Fully Crystalline Faceted Fe-Au Core-Shell Nanoparticles. *Nano Lett.* **2015**, *15*, 5075−5080.
(9) Bochicchio, D.; Ferrando, R. Morphological Instability of Core-Shell Metallic Nanoparticles. *Phys. Rev. B: Condens. Matter Mater. Phys.* **2013**, *87*, 165435.
(10) Langlois, C.; Li, Z. L.; Yuan, J.; Alloyeau, D.; Nelayah, J.; Bochicchio, D.; Ferrando, R.; Ricolleau, C. Transition from Core-Shell to Janus Chemical Configuration for Bimetallic Nanoparticles. *Nanoscale* **2012**, *4*, 3381.
(11) Chen, M.; Yamamuro, S.; Farrell, D.; Majetich, S. A. Gold-Coated Iron Nanoparticles for Biomedical Applications. *J. Appl. Phys.* **2003**, *93*, 7551.
(12) Huber, D. Synthesis, Properties, and Applications of Iron Nanoparticles. *Small* **2005**, *1*, 482−501.
(13) Daw, M. S.; Foiles, S.; Baskes, M. I. The Embedded-Atom Method: a Review of Theory and Applications. *Mater. Sci. Rep.* **1993**, *9*, 251.
(14) Cleri, F.; Rosato, V. Tight-Binding Potentials for Transition Metals and Alloys. *Phys. Rev. B: Condens. Matter Mater. Phys.* **1993**, *48*, 22.
(15) Aguado, A. In *Modeling the Electronic and Geometric Structure of Nanoalloys*; Calvo, F., Ed.; Elsevier: Amsterdam, 2013.
(16) Mendelev, M. I.; Han, S.; Srolovitz, D. J.; Ackland, G. J.; Sun, D. Y.; Asta, M. Development of New Interatomic Potentials Appropriate for Crystalline and Liquid Iron. *Philos. Mag.* **2003**, *83*, 3977−3994.
(17) Ackland, G. J.; Bacon, D. J.; Calder, A. F.; Harry, T. Computer Simulation of Point Defect Properties in Dilute Fe-Cu Alloy Using a Many-Body Interatomic Potential. *Philos. Mag. A* **1997**, *75*, 713−732.
(18) Dudarev, S. L.; Derlet, P. M. A 'Magnetic' Interatomic Potential for Molecular Dynamics Simulations. *J. Phys.: Condens. Matter* **2005**, *17*, 7097.
(19) Zhou, X. W.; Johnson, R. A.; Wadley, H. N. G. Misfit-Energy-Increasing Dislocations in Vapor-Deposited CoFe/NiFe Multilayers. *Phys. Rev. B: Condens. Matter Mater. Phys.* **2004**, *69*, 144113.
(20) Zientarski, T.; Chocyk, D. Structure and Stress in Cu/Au and Fe/Au Systems: A Molecular Dynamics Study. *Thin Solid Films* **2014**, *562*, 347−352.
(21) Hong, S.; Rahman, T. S. Geometric and Electronic Structure and Magnetic Properties of Fe-Au Nanoalloys: Insights from *Ab Initio* Calculations. *Phys. Chem. Chem. Phys.* **2015**, *17*, 28177−28185.
(22) Perdew, J. P.; Burke, K.; Ernzerhof, M. Generalized Gradient Approximation Made Simple. *Phys. Rev. Lett.* **1996**, *77*, 3865−3868.
(23) Perdew, J.; Ruzsinszky, A.; Csonka, G. I.; Vydrov, O. A.; Scuseria, G. E.; Constantin, L. A.; Zhou, X.; Burke, K. Restoring the Density-Gradient Expansion for Exchange in Solids and Surfaces. *Phys. Rev. Lett.* **2008**, *100*, 136406.
(24) Chamati, H.; Papanicolaou, N. I. Second-Moment Interatomic Potential for Gold and its Application to Molecular-Dynamics Simulations. *J. Phys.: Condens. Matter* **2004**, *16*, 8399−8407.
(25) Johnson, R. A. Alloy Models with the Embedded-Atom Method. *Phys. Rev. B: Condens. Matter Mater. Phys.* **1989**, *39*, 12554−12559.
(26) Kresse, G.; Joubert, D. From Ultrasoft Pseudopotentials to the Projector Augmented-Wave Method. *Phys. Rev. B: Condens. Matter Mater. Phys.* **1999**, *59*, 1758−1775.
(27) Blochl, P. E. Projector Augmented-Wave Method. *Phys. Rev. B: Condens. Matter Mater. Phys.* **1994**, *50*, 17953−17979.
(28) Kresse, G.; Hafner, J. Ab Initio Molecular Dynamics for Liquid Metals. *Phys. Rev. B: Condens. Matter Mater. Phys.* **1993**, *47*, 558−561.
(29) Kresse, G.; Furthmuller, J. Efficient Iterative Schemes for *Ab Initio* Total-Energy Calculations Using a Plane-Wave Basis Set. *Phys. Rev. B: Condens. Matter Mater. Phys.* **1996**, *54*, 11169−11186.
(30) Kresse, G.; Furthmuller, J. Efficiency of Ab-Initio Total Energy Calculations for Metals and Semiconductors Using a Plane-Wave Basis Set. *Comput. Mater. Sci.* **1996**, *6*, 15−50.
(31) Dewaele, A.; Torrent, M.; Loubeyre, P.; Mezouar, M. Compression Curves of Ttransition Metals in the Mbar Range: Experiments and Projector Augmented-Wave Calculations. *Phys. Rev. B: Condens. Matter Mater. Phys.* **2008**, *78*, 104102.
(32) Tyson, W.; Miller, W. Surface Free Energies of Solid Metals: Estimation from Liquid Surface Tension Measurements. *Surf. Sci.* **1977**, *62*, 267−276.
(33) Kittel, C. *Introduction to Solid State Physics*, 8th ed.; Wiley & Sons: New York, 2005.
(34) Tsuchiya, T.; Kawamura, K. Ab Initio Study of Pressure Effect on Elastic Properties of Crystalline Au. *J. Chem. Phys.* **2002**, *116*, 2121−2124.
(35) De Boer, F. R.; Boom, R.; Mattens, W. C. M.; Miedema, A. R.; Niessen, A. K. In *Cohesion and structure: Cohesion in Metals: Transition Metal Alloys*; De Boer, F. R., Pettifor, D. G., Eds.; North Holland: Amsterdam, 1989; Vol. *1*.
(36) Zhang, H. L.; Lu, S.; Punkkinen, M. P. J.; Hu, Q.-M.; Johansson, B.; Vitos, L. Static Equation of State of bcc Iron. *Phys. Rev. B: Condens. Matter Mater. Phys.* **2010**, *82*, 132409.
(37) Miedema, A. R. Surface Energies of Solid Metals. *Z. Metallkd.* **1978**, *69*, 287−292.
(38) Neighbours, J. R.; Alers, G. A. Elastic Constants of Silver and Gold. *Phys. Rev.* **1958**, *111*, 707−712.
(39) Dion, M.; Rydberg, H.; Schröder, E.; Langreth, D. C.; Lundqvist, B. I. Van der Waals Density Functional For General Geometries. *Phys. Rev. Lett.* **2004**, *92*, 246401.
(40) Klimeš, J.; Bowler, D. R.; Michaelides, A. Chemical Accuracy for the van der Waals Density Functional. *J. Phys.: Condens. Matter* **2010**, *22*, 022201.
(41) Methfessel, M.; Paxton, A. T. High-Precision Sampling for Brillouin-Zone Integration in Metals. *Phys. Rev. B: Condens. Matter Mater. Phys.* **1989**, *40*, 3616−3621.
(42) Monkhorst, H. J.; Pack, J. D. Special Points for Brillouin-Zone Integrations. *Phys. Rev. B* **1976**, *13*, 5188−5192.
(43) Benoit, M.; Langlois, C.; Combe, N.; Tang, H.; Casanove, M.-J. Structural and Electronic Properties of the Au(001)/Fe(001) Interface from Density Functional Theory Calculations. *Phys. Rev. B: Condens. Matter Mater. Phys.* **2012**, *86*, 075460.
(44) Jellinek, J.; Krissinel, E. B. Ni_nAl_m Alloy Clusters: Analysis of Structural Forms and Their Energy Ordering. *Chem. Phys. Lett.* **1996**, *258*, 283−292.
(45) Ferrando, R.; Fortunelli, A.; Rossi, G. Quantum Effects on the Structure of Pure and Binary Metallic Nanoclusters. *Phys. Rev. B: Condens. Matter Mater. Phys.* **2005**, *72*, 085449.
(46) Barcaro, G.; Sementa, L.; Fortunelli, A. A Grouping Approach to Homotop Global Optimization in Alloy Nanoparticles. *Phys. Chem. Chem. Phys.* **2014**, *16*, 24256−25265.
(47) Okamoto, H.; Massalski, T. B.; Swartzendruber, L. J.; Beck, P. A. The Au-Fe (Gold-Iron) System. *Bull. Alloy Phase Diagrams* **1984**, *5*, 592−601.
(48) Benoit, M.; Combe, N.; Ponchet, A.; Morillo, J.; Casanove, M.-J. Strain Effects on the Structural, Magnetic, and Thermodynamic Properties of the Au(001)/Fe(001) Interface from First Principles. *Phys. Rev. B: Condens. Matter Mater. Phys.* **2014**, *90*, 165437.
(49) von Goldbeck, O. K., Ed. *IRON-Binary Phase Diagrams*; Springer-Verlag: Berlin, Heidelberg, 1982; pp 13−14.
(50) Swendsen, R. H.; Wang, J.-S. Replica Monte Carlo Simulation of Spin-Glasses. *Phys. Rev. Lett.* **1986**, *57*, 2607.
(51) Geyer, G. In *Markov Chain Monte Carlo Maximum Likelihood*; Keramidas, E. K., Ed.; Inferface Foundation: Fairfax Station, 1991; p 156.
(52) Kofke, D. A. On the Acceptance Probability of Replica-Exchange Monte Carlo Trials. *J. Chem. Phys.* **2002**, *117*, 6911−6914.
(53) Predescu, C.; Predescu, M.; Ciobanu, C. V. On the Efficiency of Exchange in Parallel Tempering Monte Carlo Simulations. *J. Phys. Chem. B* **2005**, *109*, 4189−4196.
(54) Calvo, F. All-Exchanges Parallel Tempering. *J. Chem. Phys.* **2005**, *123*, 124106.
(55) Labastie, P.; Whetten, R. L. Statistical Thermodynamics of the Cluster Solid-Liquid Transition. *Phys. Rev. Lett.* **1990**, *65*, 1567−1570.
(56) Kumar, S.; Bouzida, D.; Swendsen, R. H.; Rosenberg, J. M.; Kollman, P. A. The Weighted Histogram Analysis Method for Free-

DOI: 10.1021/acs.jpcc.6b12551
J. Phys. Chem. C 2017, 121, 4680−4691

Energy Calculations on Biomolecules. I. The Method. *J. Comput. Chem.* **1992**, *13*, 1011−1021.
(57) Calvo, F. Solid-Solution Precursor to Melting in Onion-Ring Pd-Pt Nanoclusters: a Case of Second-Order-Like Phase Change? *Faraday Discuss.* **2008**, *138*, 75−88.
(58) Calvo, F. Thermodynamics of Nanoalloys. *Phys. Chem. Chem. Phys.* **2015**, *17*, 27922−27939.
(59) Calvo, F.; Fortunelli, A.; Negreiros, F.; Wales, D. J. Kinetics of Chemical Ordering in Ag-Au and Ag-Ni Nanoalloys. *J. Chem. Phys.* **2013**, *139*, 111102.
(60) Kreibig, Y.; Vollmer, M. *Optical Properties of Metal Clusters*; Springer-Verlag: Berlin, 1995.
(61) Hodak, J. H.; Henglein, A.; Giersig, M.; Hartland, G. V. Laser-Induced Inter-Diffusion in AuAg Core-Shell Nanoparticles. *J. Phys. Chem. B* **2000**, *104*, 11708−11718.
(62) Portales, H.; Saviot, L.; Duval, E.; Gaudry, M.; Cottancin, E.; Pellarin, M.; Lermé, J.; Broyer, M. Resonant Raman Scattering by Quadrupolar Vibrations of Ni-Ag Core-Shell Nanoparticles. *Phys. Rev. B: Condens. Matter Mater. Phys.* **2002**, *65*, 165422.
(63) Ristić, D.; Ivanda, M.; Furić, K.; Desnica, U. V.; Buljan, M.; Montagna, M.; Ferrari, M.; Chiasera, A.; Jestin, Y. Raman Scattering on Quadrupolar Vibrational Modes of Spherical Nanoparticles. *J. Appl. Phys.* **2008**, *104*, 073519.
(64) Burgin, J.; Langot, P.; Arbouet, A.; Margueritat, J.; Gonzalo, J.; Afonso, C. N.; Vallée, F.; Mlayah, A.; Rossell, M. D.; Van Tendeloo, G. Acoustic Vibration Modes and Electron-Lattice Coupling in Self-Assembled Silver Nanocolumns. *Nano Lett.* **2008**, *8*, 1296−1302.
(65) Olivier, S.; Conte, R.; Fortunelli, A. Derivation of an Empirical Potential for Gold with Angular Corrections. *Phys. Rev. B: Condens. Matter Mater. Phys.* **2008**, *77*, 054104.
(66) Ryu, S.; Weinberger, C. R.; Baskes, M. I.; Cai, W. Improved Modified Embedded-Atom Method Potentials for Gold and Silicon. *Modell. Simul. Mater. Sci. Eng.* **2009**, *17*, 075008.

DOI: 10.1021/acs.jpcc.6b12551
J. Phys. Chem. C 2017, 121, 4680−4691